

Strain tuning of the transport gap and magnetic order in Dirac fermion systems

Jingyao Meng(孟敬尧), Zenghui Fan(范增辉), Miao Ye(叶苗), and Tianxing Ma(马天星)
Citatio: Chin. Phys. B, 2025, 34 (**9**): 098101. DOI: 10.1088/1674-1056/adea5e
http://cpb.iphy.ac.cn; http://iopscience.iop.org/cpb

What follows is a list of articles you may be interested in

High-pressure studies on quasi-one-dimensional systems

Wenhui Liu(刘雯慧), Jiajia Feng(冯嘉嘉), Wei Zhou(周苇), Sheng Li(李升), and Zhixiang Shi(施智祥)
Chin. Phys. B, 2025, 34 (**8**): 088104. DOI: 10.1088/1674-1056/ade8dd

High pressure growth of transition-metal monosilicide RhGe single crystals

Xiangjiang Dong(董祥江), Bowen Zhang(张博文), Xubin Ye(叶旭斌), Peng Wei(魏鹏), Lei Lian(廉磊), Ning Sun(孙宁), Youwen Long(龙有文), Shangjie Tian(田尚杰), Shouguo Wang(王守国), Hechang Lei(雷和畅), and Runze Yu(于润泽)
Chin. Phys. B, 2025, 34 (**8**): 088101. DOI: 10.1088/1674-1056/add7ab

Single crystal growth and transport properties of narrow-bandgap semiconductor RhP_2

De-Sheng Wu(吴德胜), Ping Zheng(郑萍), and Jian-Lin Luo(雒建林)
Chin. Phys. B, 2024, 33 (**8**): 088101. DOI: 10.1088/1674-1056/ad4cd5

A synaptic transistor with $NdNiO_3$

Xiang Wang(汪翔), Chen Ge(葛琛), Ge Li(李格), Er-Jia Guo(郭尔佳), Meng He(何萌), Can Wang(王灿), Guo-Zhen Yang(杨国桢), Kui-Juan Jin(金奎娟)
Chin. Phys. B, 2020, 29 (**9**): 098101. DOI: 10.1088/1674-1056/aba60c

Preparation and modification of VO_2 thin film on R-sapphire substrate by rapid thermal process

Zhu Nai-Wei (朱乃伟), Hu Ming (胡明), Xia Xiao-Xu (夏晓旭), Wei Xiao-Ying (韦晓莹), Liang Ji-Ran (梁继然)
Chin. Phys. B, 2014, 23 (**4**): 048108. DOI: 10.1088/1674-1056/23/4/048108

RAPID COMMUNICATION

Strain tuning of the transport gap and magnetic order in Dirac fermion systems

Jingyao Meng(孟敬尧)[1,†], Zenghui Fan(范增辉)[1,†], Miao Ye(叶苗)[2], and Tianxing Ma(马天星)[1,3,‡]

[1] *School of Physics and Astronomy, Beijing Normal University, Beijing* 100875, *China*
[2] *Guangxi Key Laboratory of Precision Navigation Technology and Application, Guilin University of Electronic Technology, Guilin* 541004, *China*
[3] *Key Laboratory of Multiscale Spin Physics (Ministry of Education), Beijing Normal University, Beijing* 100875, *China*

(Received 13 June 2025; revised manuscript received 19 June 2025; accepted manuscript online 1 July 2025)

Using the determinant quantum Monte Carlo method, we explore a rich phase diagram featuring strain-induced metal–insulator and magnetic phase transitions in an interacting two-dimensional Dirac fermion system. Asymmetric strain applied along the zigzag crystal direction drives the semimetallic regime into a band-insulating phase, or it breaks the antiferromagnetic order of the Mott insulator, inducing a nonmagnetic insulating phase under strong correlations. The critical strain required for band gap opening or for a transport phase transition is significantly reduced in the presence of Coulomb repulsion, while increasing interaction strength makes it more difficult for strain to induce a nonmagnetic phase transition. In addition, we measure in detail the band gap modulation by strain and identify a doping effect whereby doping inhibits band gap opening. Our results provide an effective way to tune the transport gap, which could help extend the applications of graphene, whose zero band gap currently limits its use.

Keywords: strained graphene, Hubbard model, metal–insulator transition, magnetism

PACS: 81.05.ue, 71.10.Fd, 68.35.Gy

DOI: 10.1088/1674-1056/adea5e **CSTR:** 32038.14.CPB.adea5e

1. Introduction

The absence of a native band gap in graphene remains a critical barrier to its integration into high-performance electronic and optoelectronic devices, such as field-effect transistors[1,2] and infrared photodetectors.[3,4] While recent breakthroughs in moiré superlattices of twisted bilayer graphene (TBG)[5–8] have unlocked exotic quantum phases — including superconductivity,[9,10] correlated insulating states,[11] and flat bands[12] — their practical implementation is hindered by extreme sensitivity to twist angles ($\lesssim 1^\circ$) and susceptibility to disorder. Thus, the controllability of graphene, especially regarding electronic correlations, has attracted tremendous interest.[13] Graphene demonstrates exceptional mechanical robustness, sustaining uniaxial tensile stresses exceeding 130 GPa while maintaining elastic deformations up to 25% strain before fracture.[14] With such advantages, strain engineering emerges as a robust alternative, enabling deterministic control of graphene's electronic properties through mechanically tunable lattice deformations without requiring atomic-scale precision.[15–18]

Recent breakthroughs underscore strain's unique capability to bridge fundamental physics and device functionality. For example, experimentally, *in situ* strain modulation in graphene transistors has improved carrier mobility by suppressing disorder,[19] while programmable three-dimensional (3D) printed graphene architectures exploit strain to regulate electron tunneling.[20] Theoretically, advances in strain engineering have proposed diverse strain configurations to tailor graphene's electronic and magnetic properties. First-principles calculations demonstrate that biaxial tensile strain opens a band gap while inducing an antiferromagnetic (AFM) insulator transition.[21] Quantum Monte Carlo studies further reveal that isotropic strain drives competing phase transitions — either to an AFM insulating state or to a dimerized lattice configuration — depending on interaction strength.[22,23] For asymmetrical deformations, elliptic Gaussian out-of-plane distortions in graphene quantum dots enable strain-dependent carrier localization that tunes conductivity,[24] while sinusoidal inhomogeneous strain achieves site-selective magnetization control at zigzag edges, effectively creating spin-semiconducting behavior.[25] These advances highlight, at the device level: (i) strain geometry as a pivotal tool for functionalizing graphene-based materials; and (ii) the urgent need to establish quantitative relationships between strain parameters and functional outputs, such as band gap tuning and magnetic phase control.

Here, we address these key issues by combining determinant quantum Monte Carlo (DQMC) simulations[26–30] with a strained Hubbard model on a honeycomb lattice. Our results reveal a universal phase diagram (Fig. 1), demonstrating both a metal–insulator transition (MIT) and a magnetic transition.

[†] These authors contributed equally to this work.
[‡] Corresponding author. E-mail: txma@bnu.edu.cn
© 2025 Chinese Physical Society and IOP Publishing Ltd. All rights, including for text and data mining, AI training, and similar technologies, are reserved.

Considering the uniaxial strain limit of 25%, the asymmetrical third-order strain formulation (Eq. (3)) along the zigzag direction makes it possible to tune electronic and magnetic properties with the predicted on-site interaction of graphene $U/t = 2$–5.[31–34] For $U/t = 3$,[35] the threshold for band gap opening occurs at an average strain of 2.25%, suggesting symmetry breaking in graphene.[36] The thresholds for band gap opening and magnetic transition clearly demonstrate opposite electron-correlation dependences. Furthermore, theoretical calculations are conducted to elucidate strain-induced band gap modulation, while also indicating that doping elevates the strain threshold for band gap opening. These results provide a possible route to guide the design of strain-engineered graphene transistors, sensors, or spintronic devices.

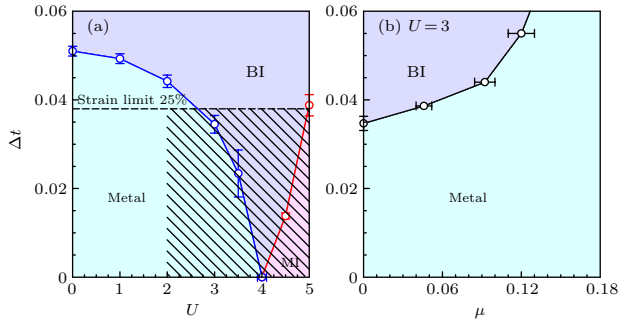


Fig. 1. Phase diagram of the strained honeycomb superlattice: (a) competing phases among metal, band insulator (BI), and Mott insulator (MI) at half-filling under the interplay of on-site interaction U and strain parameter Δt, which includes a graphene-supported region (slashed area) under the 25% strain limit; and (b) the doping effect with Δt at $U = 3$. The critical points are derived from conductivity and AFM spin structure factor in (a), and from DOS with varying μ in (b).

Figure 1 presents the unified phase diagram of strained graphene, integrating transport and magnetic properties across interaction (U), strain (Δt), and chemical potential (μ) domains. The critical points are based on the data of conductivity, AFM spin structure factor, and Fermi-level DOS with varying μ. At half-filling, a strain-induced nonmagnetic band insulator emerges from the Mott quantum critical point, corresponding to experimentally realizable graphene parameters indicated by the shaded region in Fig. 1(a). This strained graphene system establishes a practical theoretical reference by quantifying the critical strain thresholds for bandgap opening and magnetic transitions, providing essential guidance for designing graphene-based electronic and spintronic devices. Significant critical strains from Fig. 1(a) are listed in Table 1 for reference. Additionally, doping is explored as an alternative regulation approach, which suppresses bandgap opening, as shown in Fig. 1(b).

Table 1. Critical strain values in the slash of Fig. 1(a).

U	Δt (Δz)	$\varepsilon_{\rm in}$	$\varepsilon_{\rm b}$	$\varepsilon_{\rm ave}$
3.0	0.0345(0.414)	0–1.30%	22.95%	2.25%
3.5	0.0234(0.319)	0–0.70%	12.85%	1.25%
4.5	0.0138(0.233)	0–0.42%	7.84%	0.76%

2. Model and method

The Hubbard model for a honeycomb lattice with asymmetrical strain is defined as

$$\hat{H} = -\sum_{\langle ij\rangle\sigma} t_{ij}(\hat{c}^{\dagger}_{i\sigma}\hat{c}_{j\sigma} + \hat{c}^{\dagger}_{j\sigma}\hat{c}_{i\sigma}) + U\sum_{j}(\hat{n}_{j\uparrow} - \frac{1}{2})(\hat{n}_{j\downarrow} - \frac{1}{2}) - \sum_{j\sigma}\mu\hat{n}_{j\sigma}, \quad (1)$$

where $\hat{c}^{\dagger}_{i\sigma}$ ($\hat{c}_{i\sigma}$) is the spin-σ electron creation (annihilation) operator at site i, and $\hat{n}_{i\sigma} = \hat{c}^{\dagger}_{i\sigma}\hat{c}_{i\sigma}$ is the occupation number operator. Here, $U > 0$ represents the on-site Coulomb repulsive interaction, and μ is the chemical potential. To construct the strained superlattice, we define the nearest-neighbor (NN) hopping integral as

$$t_{ij} = t_0\, \mathrm{e}^{-\beta_0 \frac{\delta_a}{a_0}}, \quad (2)$$

where $t_0 = 1$ sets the energy scale ($t_0 \approx 2.8$ eV[33,37]), a_0 is the carbon–carbon bond length, $\beta_0 \approx 3$ characterizes strain sensitivity,[38,39] and $\delta_a = a' - a_0$ quantifies bond elongation (Fig. 2(a)). The out-of-plane deformation profile is given by

$$z(x,y) = \Delta z \times \left(\frac{x - x_0}{l_x/2}\right)^3, \quad (3)$$

with x_0 marking the lattice center, l_x the system length along the zigzag (x) direction, and Δz controlling the deformation amplitude (Fig. 2(b)). Figure 2(c) illustrates the strain-dependent hopping modulation for $\Delta z = 0.5$ for clarity.

We introduce a dimensionless strain parameter $\Delta t = \sum_{\langle ij\rangle}(t_0 - t_{ij})/(3L^2)$, defined as the normalized average hopping modification, to characterize strain strength universally across lattice sizes. We employ a periodic honeycomb superlattice with $L = L_x$ (L_y) $= 12$ in simulations, carried out with $\Delta t \approx 0$, 0.011, 0.021, 0.033, 0.044, 0.055, 0.064, 0.073, 0.081, and 0.089 corresponding to $\Delta z = 0$, 0.2, 0.3, 0.4, 0.5, 0.6, 0.7, 0.8, 0.9, and 1, respectively. Due to the periodic boundary conditions, the maximum strain is localized at the boundaries of the superlattice. The corresponding values of strain percentage $\varepsilon = \delta_a/a_0$ are listed in Table 2 for practical reference, and additional larger strains are studied as auxiliary theoretical cases.

Table 2. Values of strain percentage corresponding to strain parameters Δz and Δt with $\varepsilon_{\rm in/b/ave}$ corresponding to the internal/boundary/average. The values of 25% strain limit at $L = 12$ are contained on the last line.

Δz	Δt	$\varepsilon_{\rm in}$	$\varepsilon_{\rm b}$	$\varepsilon_{\rm ave}$
0	0	0%	0%	0%
0.2	0.011	0–0.31%	5.83%	0.57%
0.3	0.021	0–0.69%	12.69%	1.24%
0.4	0.033	0–1.22%	21.66%	2.12%
0.5	0.044	0–1.90%	32.29%	3.19%
0.6	0.055	0–2.72%	44.22%	4.40%
0.044	0.038	0–1.47%	25%	2.53%

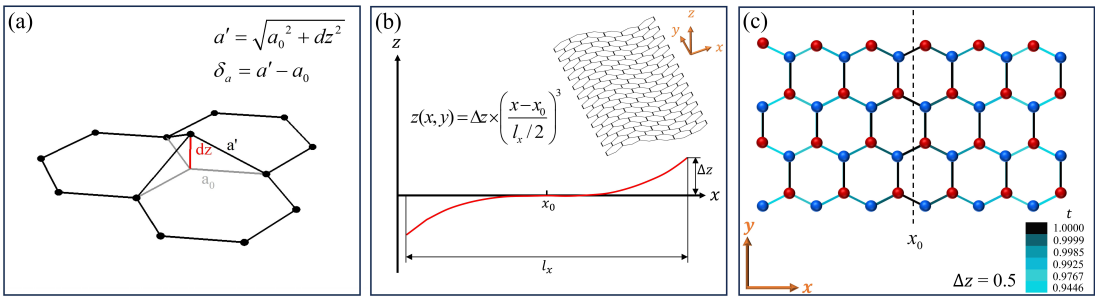


Fig. 2. A sketch of strained carbon-carbon distance in (a), where deformation occurs in the direction perpendicular to the lattice plane. (b) illustrates the form of strained honeycomb superlattice with Eq. (3), where bonds along x (zigzag) are stretched to different degrees. (c) exhibits an example with the deformation $\Delta z = 0.5$ in order to visualize hopping parameters under strain. The color of the bond reflects the magnitude of t_{ij} between NN sites: the darker the color, the closer its value is to $t_0 = 1$.

The temperature-dependent dc conductivity along the x-direction is calculated using the momentum-resolved imaginary-time current–current correlation function[27,28,40,41]

$$\sigma_{\rm dc}(T) = \frac{\beta^2}{\pi}\Lambda_{xx}\left(\boldsymbol{q} = 0,\ \ \tau = \frac{\beta}{2}\right), \tag{4}$$

where $\Lambda_{xx}(\boldsymbol{q},\tau) = \langle \widehat{j}_x(\boldsymbol{q},\tau)\widehat{j}_x(-\boldsymbol{q},0)\rangle$ with $\widehat{j}_x(\boldsymbol{q},\tau)$ denoting the x-component current operator.

The density of states (DOS) at the Fermi level, a critical indicator for distinguishing insulating mechanisms, is computed as[42,43]

$$N(0) \simeq \beta \times G(\boldsymbol{r} = 0,\ \ \tau = \beta/2), \tag{5}$$

where $G(\boldsymbol{r},\tau)$ represents the imaginary-time Green's function.

We further compute the normalized AFM spin structure factor

$$S_{\rm AFM} = \frac{1}{N}\sum_{i,j}(-1)^{(i+j)}\langle S_i S_j\rangle, \tag{6}$$

where S_i is the spin operator and the phase factor is $+1$ (-1) for sites i, j that belong to the same (different) sublattices.

Additionally, the AFM spin susceptibility is calculated to characterize magnetic properties

$$\chi_{\rm AFM} = \frac{1}{N}\sum_{i,j}(-1)^{(i+j)}\int_0^\beta \langle S_i(\tau)S_j(0)\rangle\,{\rm d}\tau. \tag{7}$$

3. Results and discussion

Application of strain to the metallic honeycomb lattice drives a metal–insulator transition (MIT) via modulation of the hopping parameter Δt. Figures 3(a)–3(c) present the T-dependent dc conductivity $\sigma_{\rm dc}$ for different strain levels (Δt) and interaction strengths (U). At low Δt, the metallic nature manifests as a diverging $\sigma_{\rm dc}$ $(T \to 0)$ with negative ${\rm d}\sigma_{\rm dc}/{\rm d}T$ at low temperatures, which is consistent with graphene's gapless band structure under weak correlations.[36] Increasing Δt systematically suppresses $\sigma_{\rm dc}(T)$. The crossover to insulating behavior, where $\sigma_{\rm dc}$ increases with T, is clearly demonstrated in Figs. 3(a)–3(c), confirming the strain-driven MIT. The critical point $\Delta t_{\rm c}$ is identified at ${\rm d}\sigma_{\rm dc}/{\rm d}T = 0$.

The critical strain threshold $\Delta t_{\rm c}$ shows pronounced dependence on interaction strength U, as revealed by the $\sigma_{\rm dc}$ versus Δt curves in Figs. 3(d)–3(f). Across all parameter regimes, $\sigma_{\rm dc}$ decreases monotonically with strain, exhibiting steeper suppression at larger β — a hallmark of stronger strain-induced suppression of conductivity in the low-T limit. The transition points $\Delta t_{\rm c}$, marked by vertical dashed lines at the intersection of $\sigma_{\rm dc}(\Delta t)$ curves, systematically shift leftward with increasing U, directly correlating interaction strength with reduced critical strain. These results establish U and Δt as competing mechanisms for the MIT.

The $\sigma_{\rm dc}$ analysis identifies metal–insulator phase boundaries but leaves the insulating state's origin unresolved. To address this, Figs. 3(g)–3(h) present the DOS at the Fermi level $N(0)$, revealing band insulating behavior. By tracking $N(0)$ versus T near the MIT boundary and performing linear extrapolations to $T \to 0$, we establish the evolution of the bandgap in the thermodynamic limit. These results align quantitatively with conductivity measurements — as Δt increases, $N(0)_{T\to 0}$ diminishes systematically, vanishing at $\Delta t \sim 0.033$ for $U = 3$ (Fig. 3(h)), confirming strain-induced bandgap opening.[44] While small discrepancies exist between conductivity-derived and $N(0)$-determined critical $\Delta t_{\rm c}$, their close agreement validates the simultaneous emergence of the MIT and the bandgap. This consistency confirms the insulating phase as a conventional band insulator.

The pristine honeycomb Hubbard model exhibits a well-documented quantum phase transition from paramagnetic metal to antiferromagnetic Mott insulator at $U_{\rm c} \approx 4.0$.[27,45–49] To investigate strain's potential role in enhancing AFM order under weak interactions $(U < U_{\rm c})$, Figs. 3(i) and 3(j) present the AFM spin susceptibility $\chi_{\rm AFM}(T)$ for $U = 2$ and 3 across multiple strain levels. Notably, $\chi_{\rm AFM}$ profiles are indistinguishable from the $\Delta t = 0$ baseline at all strain levels — particularly below $T \approx 0.1$ — demonstrating the negligible impact of strain on AFM fluctuations. This invariance confirms the persistence of $\Delta t = 0$ magnetic characteristics at weak coupling, with large Δt ultimately stabilizing a nonmagnetic band insulator.

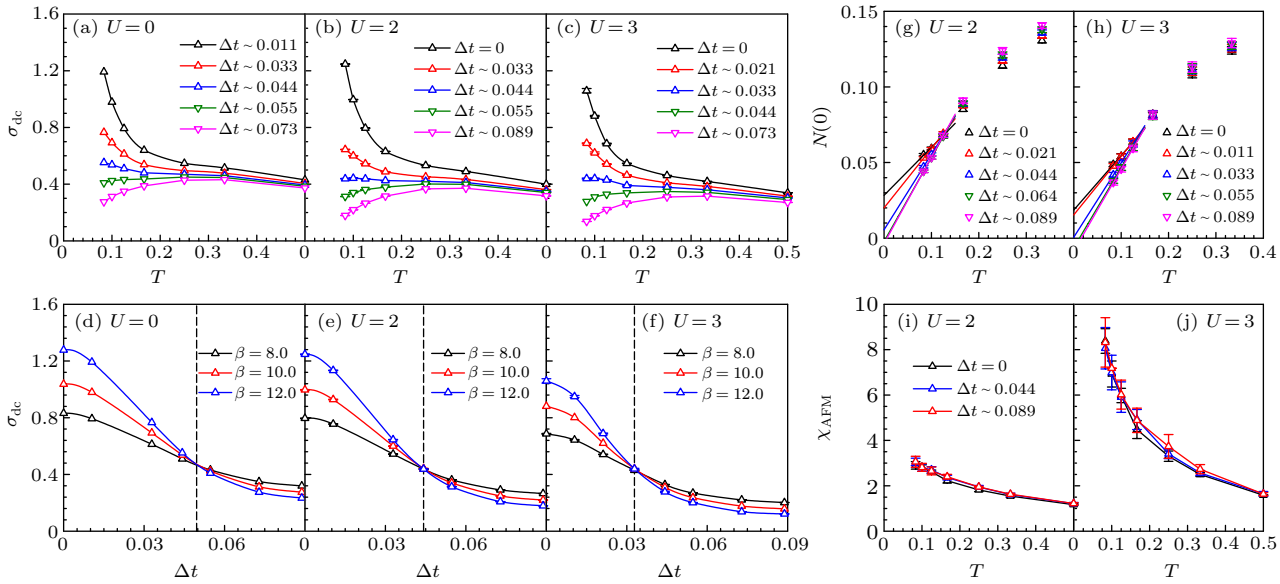


Fig. 3. (a)–(c) Temperature dependence of the dc conductivity σ_{dc} for various Δt at $U = 0$, 2, and 3. At small Δt, σ_{dc} decreases with increasing T, indicating metallic behavior, whereas at larger Δt, σ_{dc} increases with T, characteristic of an insulating state. (d)–(f) σ_{dc} as a function of Δt for several inverse temperatures β at $U = 0$, 2, and 3. The suppression of σ_{dc} by strain is more pronounced at low temperatures, and the critical value Δt_c decreases with increasing U, taking values of approximately 0.050, 0.044, and 0.033 for $U = 0$, 2, and 3, respectively. (g)–(h) Density of states at the Fermi level, $N(0)$, as a function of T at (g) $U = 2.0$ and (h) $U = 3.0$. Low-temperature data are linearly extrapolated; the vanishing intercept in the thermodynamic limit signals the opening of a bandgap. (i)–(j) Antiferromagnetic susceptibility χ_{AFM} as a function of T for various Δt at (i) $U = 2$ and (j) $U = 3.0$, including the unstrained case ($\Delta t = 0$). The curves for different Δt nearly overlap under both interaction strengths, suggesting that strain has negligible influence on χ_{AFM}.

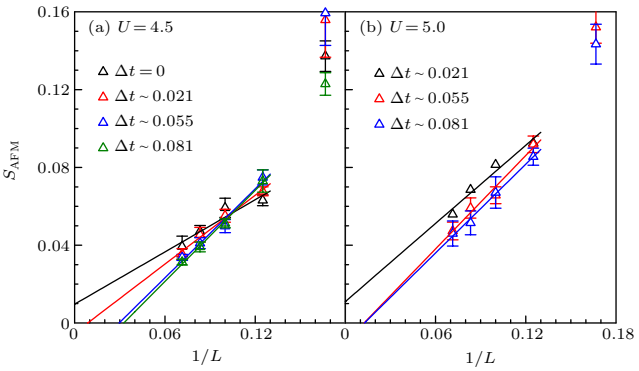


Fig. 4. S_{AFM} as a function of inverse lattice size $1/L$ for various Δt at (a) $U = 4.5$ and (b) $U = 5$, with $L = L_x = L_y$. Data points at large L are used for linear fitting. The vanishing intercept at sufficiently large Δt indicates the absence of AFM order. The critical values are estimated as $\Delta t_c \approx 0.013$ for $U = 4.5$ and $\Delta t_c \approx 0.039$ for $U = 5.0$.

At elevated Coulomb repulsion ($U > 4.0$), the unstrained system transitions to a Mott insulator hosting AFM order and a correlation-driven Mott gap. Strain dramatically modifies this behavior, as evidenced by finite-size scaling of the AFM spin structure factor S_{AFM}. For $U = 4.5$ without strain, $S_{AFM}(1/L \to 0)$ saturates to finite values, confirming long-range magnetic order in Fig. 4(a), while applied strain progressively suppresses AFM order, leading to its complete disappearance at $\Delta t_c \sim 0.013$. This critical strain increases to $\Delta t_c \sim 0.039$ for $U = 5.0$ in Fig. 4(b), demonstrating enhanced resistance to magnetic suppression with stronger interactions. We note that significant errors arise under strong interactions; thus, linear fitting at low temperatures is employed to provide a qualitative conclusion regarding the magnetic transition. Nevertheless, the suppression of AFM order across $U = 4.5$–5.0 is robust, establishing strain as a control parameter for magnetic phases in correlated 2D materials.

Our findings establish strain as an effective tool for opening bandgaps in honeycomb superlattices, stabilizing nonmagnetic insulating phases at weak interactions ($U < U_c$). Beyond fundamental phase characterization, precise bandgap tunability holds particular significance for graphene-based electronics, enabling critical device functionalities in transistors, photodetectors, and sensor architectures where dynamically adjustable bandgaps are essential. To quantify this tunability, Fig. 5 presents strain-modulated bandgap measurements via Fermi-level DOS analysis at finite chemical potential μ.

The bandgap Δ shown in Fig. 5(a) is determined through chemical potential sweeps: starting from the half-filled insulator ($\mu = 0$), the Fermi level progressively enters the conduction band as μ increases, marked by the emergence of finite DOS at $N(0)$. We define $\Delta = 2\mu_c$ in units of t_0, where μ_c denotes the critical potential for DOS onset. For instance, linear extrapolation of $N(0)$ to the thermodynamic limit yields $\mu_c = 0.12$ for the $\Delta t \sim 0.055$ case in Fig. 5(b), yielding $\Delta = 0.24$. Error bars are calculated from adjacent μ values (0.11–0.13) in the DOS transition region of Fig. 5(b). This approach provides a useful experimental reference, establishing a quantitative bridge between theoretical models and applied bandgap engineering.

The synergistic effects of strain Δt and interaction U on bandgap evolution are quantified in Figs. 5(c) and 5(d). For fixed $U = 3$ and $\mu = 0.12$, increasing Δt from 0.044 to 0.064 progressively reduces the Fermi-level DOS (Fig. 5(c)), confirming the strain-induced widening of the bandgap. Con-

versely, at fixed $\Delta t \sim 0.064$ and $\mu = 0.06$, increasing U from 1 to 3 suppresses the Fermi-level DOS (Fig. 5(d)), demonstrating interaction-driven stabilization of the bandgap. These complementary trends reveal a cooperative mechanism where strain and interaction jointly enhance gap formation, as summarized in Fig. 5(a).

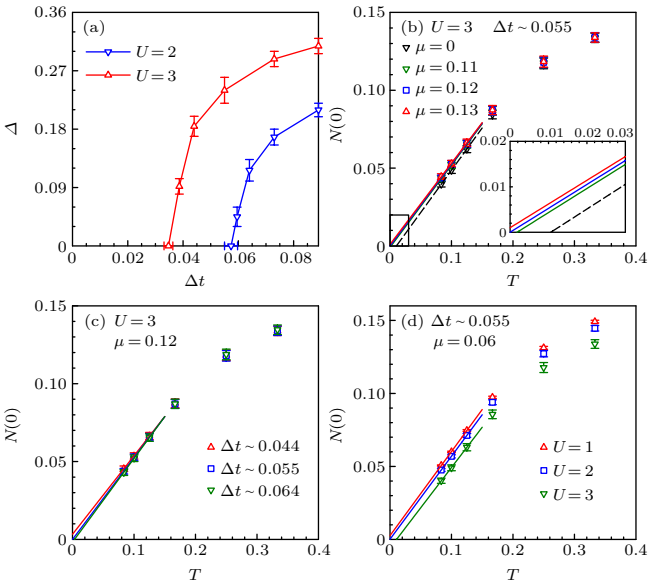


Fig. 5. (a) Bandgap Δ as a function of Δt at $U = 2$ and 3, illustrating the detailed modulation of the bandgap by strain. Δ is derived from the Fermi-level DOS $N(0)$ calculated with varying chemical potential μ. (b) Fermi-level DOS $N(0)$ as a function of T for different μ, with U and Δt fixed; the inset shows a partial enlargement. This panel exemplifies the procedure for determining Δ in (a). (c) Fermi-level DOS $N(0)$ as a function of T for different Δt, with $U = 3$ and $\mu = 0.12$ fixed, illustrating the effect of strain on the MIT. (d) Fermi-level DOS $N(0)$ as a function of T for different U, with $\Delta t \sim 0.064$ and $\mu = 0.06$ fixed, illustrating the effect of interaction strength on the MIT. In panels (b)–(d), low-temperature $N(0)$ data are extrapolated to the thermodynamic limit via linear fitting.

4. Summary

In summary, we propose an asymmetrical uniaxial strain in the form of Eq. (3) as a practical and scalable approach for controlling both electronic and magnetic phases in graphene-based correlated materials. Using DQMC simulations, we numerically investigate the effects of strain on transport and magnetic properties in graphene. The strain thresholds for bandgap opening and magnetic transitions are summarized as the boundaries of the metal–insulator and magnetic phase transitions in Fig. 1. The thresholds exhibit a clear dependence on electron correlation: increasing interaction reduces the threshold for bandgap opening but increases it for magnetic transitions. The region of experimentally accessible strain and interaction parameters, covering phase crossovers, provides guidance for designing graphene-based electronic and spintronic devices. Precise bandgap tunability favorable for graphene-based electronics is also supported by this work. Chemical doping of strained graphene further increases the strain thresholds for bandgap opening, providing an additional means of regulating the electronic properties of graphene.

This work establishes strain as a versatile and scalable tool for bandgap engineering and magnetic control in 2D materials, advancing the integration of graphene into functional devices.

Acknowledgments

This project was supported by the National Natural Science Foundation of China (Grant No. 12474218), the Beijing Natural Science Foundation (Grant No. 1242022), and the Guangxi Key Laboratory of Precision Navigation Technology and Application, Guilin University of Electronic Technology (Grant No. DH202322). The numerical simulations were performed at the High-Performance Scientific Computing Center (HSCC) of Beijing Normal University and on Tianhe-2JK at the Beijing Computational Science Research Center.

References

[1] Schwierz F 2010 *Nat. Nanotechnol.* **5** 487
[2] Sun M, Wang S, Liang Y, Wang C, Zhang Y, Liu H, Zhang Y and Han L 2025 *Nano-Micro Lett.* **17** 24
[3] Wang H, Li Z, Li D, Chen P, Pi L, Zhou X and Zhai T 2021 *Adv. Funct. Mater.* **31** 2103106
[4] Jhang A T, Tsai P C, Tsai Y T, Lin S Y and Fang M H 2024 *Adv. Opt. Mater.* **12** 2401252
[5] Cao Y, Fatemi V, Fang S, Watanabe K, Taniguchi T, Kaxiras E and Jarillo-Herrero P 2018 *Nature* **556** 43
[6] Andrei E Y and MacDonald A H 2020 *Nat. Mater.* **19** 1265
[7] Zheng Q, Hao C Y, Zhou X F, Zhao Y X, He J Q and He L 2022 *Phys. Rev. Lett.* **129** 076803
[8] Chu Y, Zhu F, Wen L, Chen W, Chen Q and Ma T 2020 *Chin. Phys. B* **29** 117401
[9] Cao Y, Rodan-Legrain D, Park J M, Yuan N F Q, Watanabe K, Taniguchi T, Fernandes R M, Fu L and Jarillo-Herrero P 2021 *Science* **372** 264
[10] Lian B, Wang Z and Bernevig B A 2019 *Phys. Rev. Lett.* **122** 257002
[11] Cao Y, Fatemi V, Demir A, Fang S, Tomarken S L, Luo J Y, Sanchez-Yamagishi J D, Watanabe K, Taniguchi T, Kaxiras E, Ashoori R C and Jarillo-Herrero P 2018 *Nature* **556** 80
[12] Dong K, Zhang T, Li J, Wang Q, Yang F, Rho Y, Wang D, Grigoropoulos C P, Wu J and Yao J 2021 *Phys. Rev. Lett.* **126** 223601
[13] Zhang S, Dai X and Liu J 2022 *Phys. Rev. Lett.* **128** 026403
[14] Lee C, Wei X, Kysar J W and Hone J 2008 *Science* **321** 385
[15] Si C, Sun Z and Liu F 2016 *Nanoscale* **8** 3207
[16] Manesco A L R and Lado J L 2021 *2D Mater.* **8** 035057
[17] Mao J, Milovanović S P, Andelković M, Lai X, Cao Y, Watanabe K, Taniguchi T, Covaci L, Peeters F M, Geim A K, Jiang Y and Andrei E Y 2020 *Nature* **584** 215
[18] Li B, Cao Y, Xu L, Yang G, Ma Z, Ye M and Ma T 2019 *Chin. Phys. Lett.* **36** 067503
[19] Wang L, Makk P, Zihlmann S, Baumgartner A, Indolese D I, Watanabe K, Taniguchi T and Schönenberger C 2020 *Phys. Rev. Lett.* **124** 157701
[20] Carvalho Fernandes D C, Lynch D and Berry V 2020 *Sci. Rep.* **10** 11373
[21] Lee S H, Kim S and Kim K 2012 *Phys. Rev. B* **86** 155436
[22] Tang H K, Laksono E, Rodrigues J N B, Sengupta P, Assaad F F and Adam S 2015 *Phys. Rev. Lett.* **115** 186602
[23] Sorella S, Seki K, Brovko O O, Shirakawa T, Miyakoshi S, Yunoki S and Tosatti E 2018 *Phys. Rev. Lett.* **121** 066402
[24] Poszwa A 2022 *Sci. Rep.* **12** 9908
[25] Ildarabadi F and Farghadan R 2021 *Phys. Rev. B* **103** 115424
[26] White S R, Scalapino D J, Sugar R L, Loh E Y, Gubernatis J E and Scalettar R T 1989 *Phys. Rev. B* **40** 506
[27] Ma T, Zhang L, Chang C C, Hung H H and Scalettar R T 2018 *Phys. Rev. Lett.* **120** 116601
[28] Paiva T, Khatami E, Yang S, Rousseau V, Jarrell M, Moreno J, Hulet R G and Scalettar R T 2015 *Phys. Rev. Lett.* **115** 240402

[29] Zhang L, Ma C and Ma T 2021 *Phys. Status Solidi RRL* **15** 2100287
[30] Cheng S, Yu J, Ma T and Peres N M R 2015 *Phys. Rev. B* **91** 075410
[31] Gloor T and Mila F 2004 *Eur. Phys. J. B* **38** 9
[32] Herbut I F 2006 *Phys. Rev. Lett.* **97** 146401
[33] Castro Neto A H, Guinea F, Peres N M R, Novoselov K S and Geim A K 2009 *Rev. Mod. Phys.* **81** 109
[34] Wehling T O, Şaşıoğlu E, Friedrich C, Lichtenstein A I, Katsnelson M I and Blügel S 2011 *Phys. Rev. Lett.* **106** 236805
[35] Ma T, Hu F, Huang Z and Lin H Q 2010 *Appl. Phys. Lett.* **97** 112504
[36] Quan S, Zhang Y and Chen W 2022 *Phys. Chem. Chem. Phys.* **24** 23929
[37] Reich S, Maultzsch J, Thomsen C and Ordejón P 2002 *Phys. Rev. B* **66** 035412
[38] Torres V, Silva P, de Souza E A T, Silva L A and Bahamon D A 2019 *Phys. Rev. B* **100** 205411
[39] Chang Y, Albash T and Haas S 2012 *Phys. Rev. B* **86** 125402
[40] Huang E W, Sheppard R, Moritz B and Devereaux T P 2019 *Science* **366** 987
[41] Scalettar R T, Trivedi N and Huscroft C 1999 *Phys. Rev. B* **59** 4364
[42] Trivedi N and Randeria M 1995 *Phys. Rev. Lett.* **75** 312
[43] Lederer S, Schattner Y, Berg E and Kivelson S A 2017 *Proc. Natl. Acad. Sci. USA* **114** 4905
[44] Antipov A E, Javanmard Y, Ribeiro P and Kirchner S 2016 *Phys. Rev. Lett.* **117** 146601
[45] Paiva T, Scalettar R T, Zheng W, Singh R R P and Oitmaa J 2005 *Phys. Rev. B* **72** 085123
[46] Sorella S and Tosatti E 1992 *Europhys. Lett.* **19** 699
[47] Martelo L M, Dzierzawa M, Siffert L and Baeriswyl D 1996 *Z. Phys. B* **103** 335
[48] Furukawa N 2001 *J. Phys. Soc. Jpn.* **70** 1483
[49] Meng Z Y, Lang T C, Wessel S, Assaad F F and Muramatsu A 2010 *Nature* **464** 847